Solid State Sciences 122 (2021) 106771

Contents lists available at ScienceDirect

Solid State Sciences

journal homepage: www.elsevier.com/locate/ssscie

Strain and electric field tunable electronic and optical properties in antimonene/C_3N van der Waals heterostructure

Lichen Gao [a], Bin Zhou [a], Jinzhong Zhang [a], Kai Jiang [a], Liyan Shang [a,**], Zhigao Hu [a,b,c,*], Junhao Chu [a,b,c]

[a] Technical Center for Multifunctional Magneto-Optical Spectroscopy (Shanghai), Engineering Research Center of Nanophotonics & Advanced Instrument (Ministry of Education), Department of Materials, School of Physics and Electronic Science, East China Normal University, Shanghai, 200241, China
[b] Collaborative Innovation Center of Extreme Optics, Shanxi University, Taiyuan, Shanxi, 030006, China
[c] Shanghai Institute of Intelligent Electronics & Systems, Fudan University, Shanghai, 200433, China

ARTICLE INFO

Keywords:
2D carbonitride
The first principles
van der Waals heterostructure
Indirect band gap

ABSTRACT

Two-dimensional (2D) crystalline carbonitride C_3N, as a very attractive material, has received extensive attention. By using the first-principles calculations, we systematically studied the electronic properties of antimonene/C_3N van der Waals (vdW) heterojunction. The results show that the heterostructure has an inherent type-II band alignment with an indirect band gap. Moreover, the band gap of the C_3N/antimonene heterojunction can be adjusted linearly within a certain range by applying vertical strain and electric field. The calculated absorption curve shows that the antimonene/C_3N heterostructure can exhibit good visible-light absorption performance, and the optical properties of the C_3N/antimonene heterojunction can be changed by applying biaxial and vertical strain, which can be expected to have potential applications in photovoltaic devices.

1. Introduction

Graphene has started the research craze for two-dimensional (2D) materials [1]. In recent years, people have been trying to build van der Waals heterojunctions with 2D semiconductor materials such as silylene, black phosphorus, transition metal dichalcogenides (TMDCs), and MXenes [2,3]. Unfortunately, these materials are facing various application dilemmas. For example, black phosphorus and germanene are unstable when exposed to humid air, which makes them difficult to achieve large-scale practical applications [4,5], and the application of MoS_2 and WSe_2 in field effect transistors (FET) is limited due to low mobility [6]. As an attractive carbon-based 2D material with a graphene-like structure, C_3N was successfully prepared recently, and it shows that C_3N is an indirect band gap semiconductor with a narrow band gap of 0.39 eV [7]. C_3N has a wide spectral response range due to the small band gap, high carrier mobility and high on/off ratio ($\sim 10^5$) make it great application potential in FET. In addition, C_3N has good electrochemical properties and is also an ideal candidate for electrode materials [8,9]. In recent years, β-antimonene has also been proposed as a stable 2D structure. Wu et al. realized the growth of single-layer antimonene nanosheets on $PdTe_2$ substrates [10], Zeng et al. developed the van der Waals epitaxial growth method and prepared a higher-quality 2D antimonene film [11]. Compared with black phosphorus, single-layer antimonene has a higher mobility, high chemical stability in the air, and is not oxidized after exposure to air. It shows that the single-layer antimonene has an indirect band gap of about 2.28 eV, which corresponds to the energy range of the blue light, and fills the gaps in the traditional semiconductor response spectrum. In addition, applying biaxial strain can transform antimonene from an indirect band gap to a direct band gap [12]. The above results indicate that both antimonene and C_3N have broad application prospects in nanoelectronics and optical devices. Therefore, it is expected that the single-layer structure of the two materials can be stacked to form a vdW heterojunction to exhibit high stability and good optoelectronic properties.

In this work, we study the electronic and optical properties of

* Corresponding author. Technical Center for Multifunctional Magneto-Optical Spectroscopy (Shanghai), Engineering Research Center of Nanophotonics & Advanced Instrument (Ministry of Education), Department of Materials, School of Physics and Electronic Science, East China Normal University, Shanghai, 200241, China.
** Corresponding author.
E-mail addresses: lyshang@ee.ecnu.edu.cn (L. Shang), zghu@ee.ecnu.edu.cn (Z. Hu).

https://doi.org/10.1016/j.solidstatesciences.2021.106771
Received 25 July 2021; Received in revised form 7 October 2021; Accepted 31 October 2021
Available online 9 November 2021

antimonene/C_3N van der Waals heterojunction by density functional theory (DFT). The effects of vertical strain and applied electric field on the electronic properties have been discussed in details. Moreover, it indicated that the vertical strain and biaxial strain can also significantly modulate the optoelectronic properties of the heterojunction.

2. Computational details

All calculations are performed by using the Vienna ab initio simulation package (VASP) code [13,14]. The electronic exchange-correlation potential is described using the projector-augmented wave (PAW) pseudopotentials. The generalized gradient approximation (GGA) of Perdew-Burke-Ernzerhof (PBE) functional is implemented for electron exchange and correlation [15]. Consider the interlayer interaction in the antimonene/C_3N vdW heterostructure by using the semi-empirical DFT-D2 method to simulate the effect of vdW interaction [16]. The plane wave basis set with a cut-off energy of 500 eV is used for the expansion of the electronic wave function and a 15 Å vacuum region is used to simulate the isolated sheet along the z direction. Monkhorst-Pack 15 × 15 × 1 K-point grid of Brillouin zone is sampled for the relaxation of monolayer C_3N, monolayer antimonene and heterostructure [17]. During the electron self-consistent calculation, the energy convergence standard is set to 10^{-6} eV, and the calculation stops when the force on each atom is less than 0.01 eV $Å^{-1}$. In order to obtain more accurate band gap, HSE06 hybrid functional is adopted.

The basic optical properties of the heterojunction can be well characterized by the light absorption coefficient $\alpha(\omega)$ [18], which can be expressed as

$$\alpha(\omega) = \sqrt{2\omega}[\sqrt{\epsilon_1(\omega)^2 + \epsilon_2(\omega)^2} - \epsilon_1(\omega)]^{1/2} \quad (1)$$

where ϵ_1 and ϵ_2 are the real part and imaginary part of the complex dielectric function, respectively.

3. Results and discussion

3.1. Geometrically optimized structures

We first explored the geometric structure of the monolayer C_3N and monolayer antimonene. The top views of the atomic structure for the antimonene and C_3N monolayers are shown in Fig. 1(a). The optimized in-plane lattice constants for antimonene are $a = b = 4.04$ Å, and the lattice constants of C_3N are $a = b = 4.86$ Å. Both results are consistent with previous reports [19,20]. Therefore, a 2 × 2 antimonene supercell and a $\sqrt{3} \times \sqrt{3}$ C_3N supercell were chosen to construct a heterojunction. The lattice mismatch of heterojunction is only 2.56%.

In order to obtain stable heterostructures, three stacking configurations were considered (labeled I, II and III), as shown in Fig. 1(b). For configurations I and III, antimony atoms are aligned with the center of the hexagon surrounded by carbon and nitrogen atoms. In configuration II, antimony atoms lie directly below carbon and nitrogen atoms.

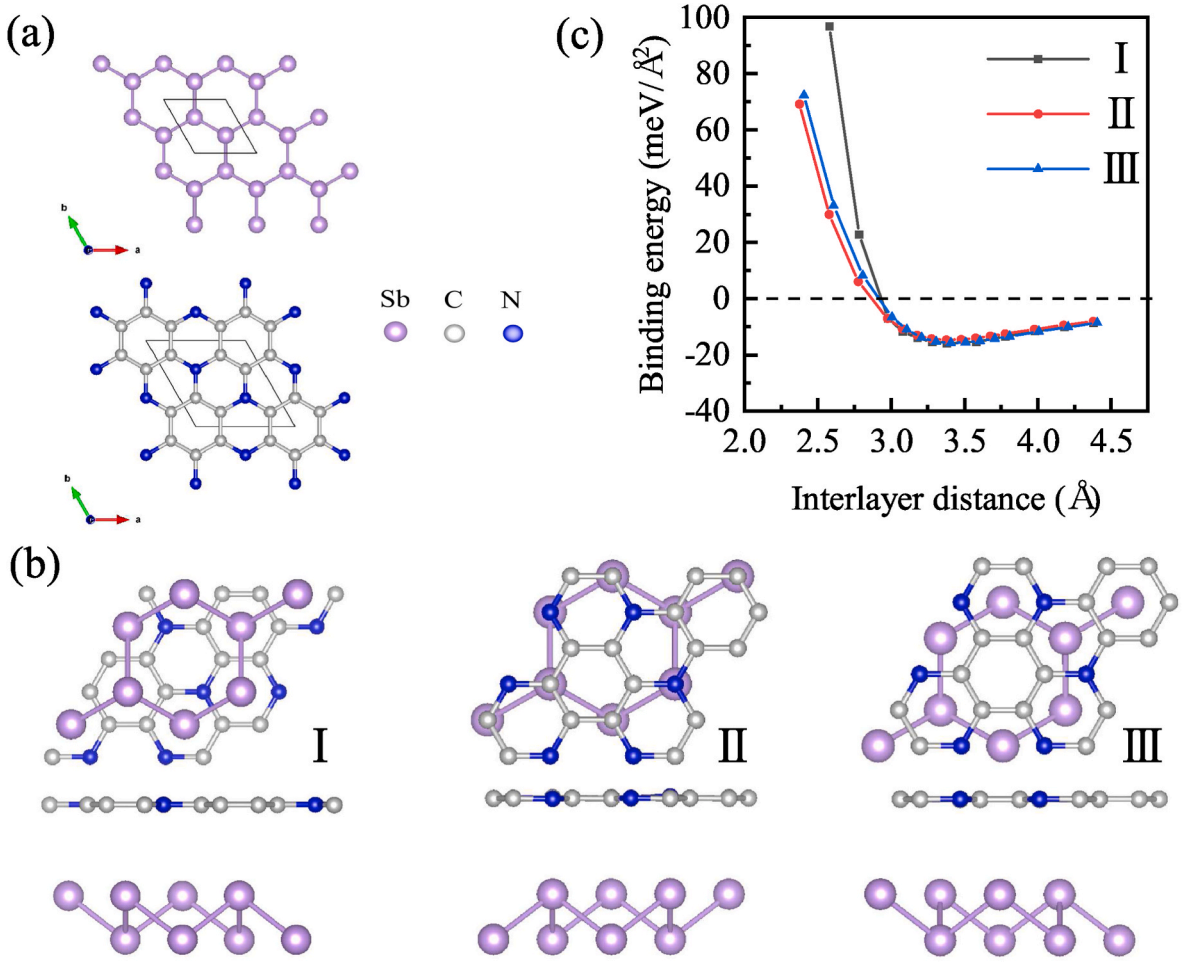

Fig. 1. (a) The top views of atomic structure of (a) antimonene and C_3N monolayers, where the dashed rectangle indicates the unit cell. (b) The top and side views of atomic structure of heterostructures with three different stacking configurations. (c) The calculated binding energies as a function of the interlayer distance for the corresponding antimonene/C_3N heterostructures.

The results show that the equilibrium distances between the C_3N and the antimonene are 3.38 Å, 3.40 Å and 3.37 Å for I, II and III, respectively, and in order to further verify the stability of antimonene/C_3N heterojunction, the corresponding binding energy changes with the distance between layers as shown in Fig. 1(c), which is defined as

$$E_b = (E_{antimonene/C_3N} - E_{C_3N} - E_{antimonene})/A \quad (2)$$

where $E_{antimonene/C_3N}$ is the total energy of the C_3N/antimonene vdW heterostructure, E_{C_3N} and $E_{antimonene}$ are the total energy of an isolated C_3N and antimonene monolayer, respectively. A is the interface area of heterostructure. The binding energy E_b reaches the minimumis (−15.9 meV/Å^2, −14.7 meV/Å^2 and −15.7 meV/Å^2 for I, II and III, respectively) at equilibrium. Therefore, configuration I has the lowest binding energy and the most stable structure, which is taken as the research object.

3.2. Electronic properties of the heterojunction

To figure out the electronic properties of antimonene/C_3N heterojunction, the electronic properties of single-layer C_3N and single-layer

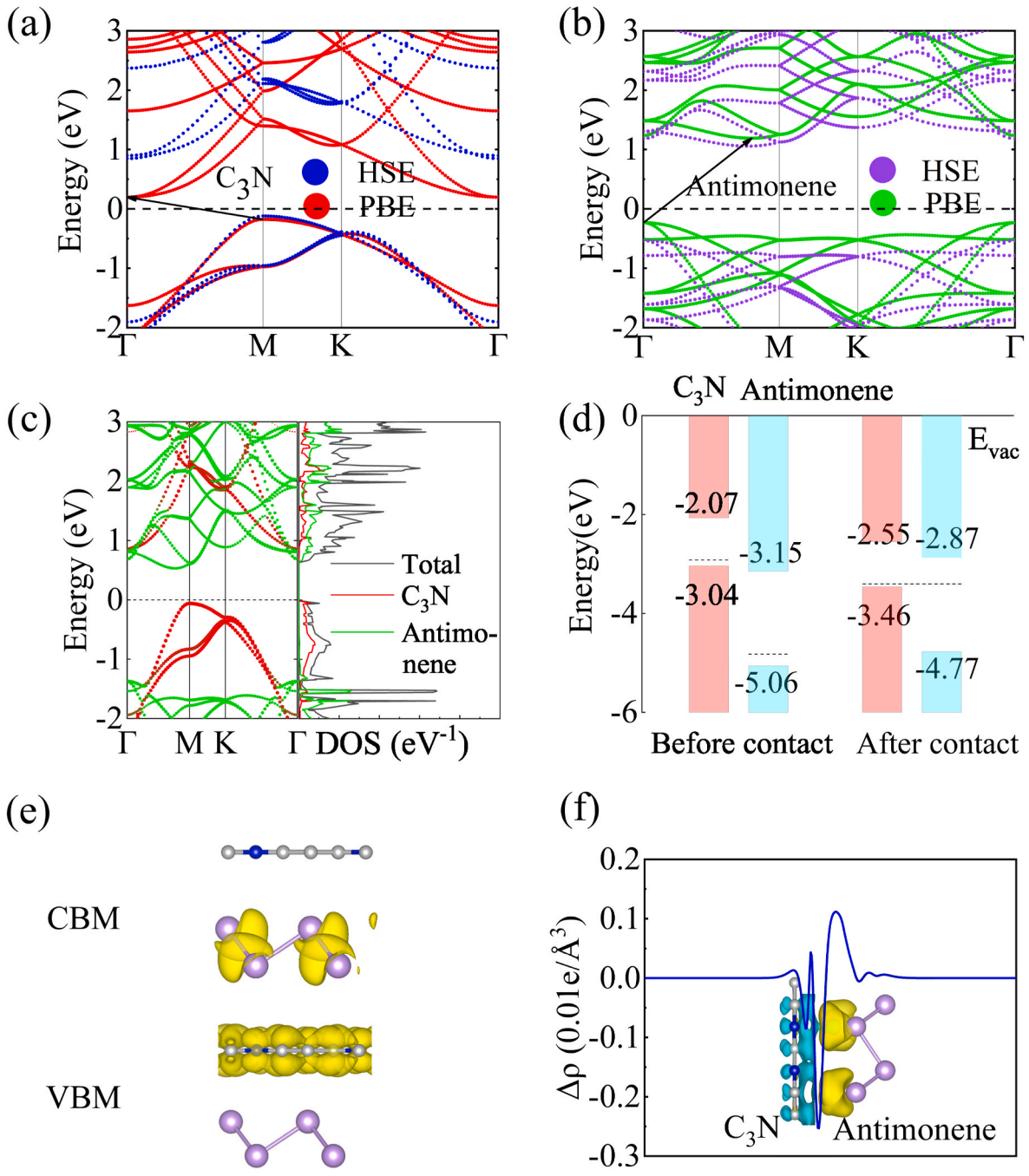

Fig. 2. The band structures for (a) the monolayer C_3N, (b) the monolayer antimonene calculated by PBE and HSE06. The Fermi level E_F is set to zero. (c) The projected band structure and PDOS of the antimonene/C_3N heterostructure calculated by HSE06. The red and green lines represent the contributions from C_3N and antimonene, respectively. (d) The band alignment of the antimonene/C_3N heterostructure. (e) The decomposition charge density of VBM and CBM. (f) The plane-averaged charge density difference of the heterostructure. The yellow and blue ares represent electrons accumulation and depletion, respectively. (For interpretation of the references to colour in this figure legend, the reader is referred to the Web version of this article.)

antimonene were calculated. The calculated band structure of the monolayer C_3N and monolayer antimonene are shown in Fig. 2(a) and (b), respectively. For the monolayer antimonene, it has an indirect bandgap of 1.42 eV (1.91 eV calculated by HSE06), while the C_3N monolayer showing a finite indirect band gap of 0.39 eV (0.97 eV calculated by HSE06). All the results are in good agreement with previous theoretical reports [6,19,21]. The calculated band structure of the heterojunction is shown in Fig. 2(c). Obviously, the band structure of heterojunction is the superposition of two single layers, which is in line with the typical characteristics of heterojunction. The antimonene/C_3N heterostructure with an indirect band gap of 0.15 eV (0.59 eV calculated by HSE06) was obtained, the bottom of the conduction band of the heterojunction is located between the Γ-point and M-point, and the top of the valence band is located at the point M-point, as listed in Table 1. The projected density of states (PDOS) is also in good agreement with the band structure. The density of states at the bottom of the conduction band is mainly contributed by antimonene, while the density of states at the top of the valence band is mainly derived from C_3N layer.

Band alignment is very important for analyzing contact interface [22,23]. The band edges of the monolayer antimonene, monolayer C_3N, and antimonene/C_3N heterostructure are presented in Fig. 2(d). It can be seen that the heterojunction has type-II band arrangement, which is expected to be practically applied in optoelectronic devices. In order to understand the distribution of charge in the heterojunction more clearly, the band decomposed charge density of antimonene/C_3N heterostructure was also calculated. Fig. 2(e) clearly show that the lowest energy electron states are located in the antimonene layer, while the lowest energy hole states are located in the C_3N layer. In addition, the work function φ (defined as the energy difference between the vacuum level E_{vac} and the Fermi level E_F) is helpful in analyzing the flow of electrons in the heterojunction. The work functions of the monolayer C_3N and the monolayer antimonene are 2.92 eV and 4.82 eV, respectively, as listed in Table 1. When the antimonene/C_3N vertical heterostructure is formed, electrons accumulate in antimonene and the holes flow spontaneously to C_3N, owing to the fact that the work function of antimonene is higher than that of C_3N. The redistribution of charge can be observed at the contact interface, as shown in Fig. 2(f). Therefore, the photogenerated electrons can easily flow from C_3N to antimonene by the conduction band minimum (CBM) offset. However, the photogenerated holes can transferer from antimonene to C_3N by the valence band maximum (VBM) offset. As a result, the antimonene/C_3N heterojunction realizes the spatial separation of electron-hole pairs and prolongs the carrier lifetime, which is expected to have good performance in optoelectronic devices [24]. Finally, a built-in electric field E_{int} is formed at the interface, the direction of E_{int} is from C_3N to antimonene. Before reaching the equilibrium position, more and more electrons accumulate in antimonene, while holes accumulate in the C_3N layer, which leads to the increase of the E_{int} and in turn inhibits the electron transfer.

3.3. Adjustment of electronic structure by vertical strain

The adjustable band gap is important for the performance of optoelectronic devices. Applying strain is a common methods to modulate the band structure of 2D materials [25]. The band structure and electronic properties of van der Waals heterojunction can be adjusted by applying vertical strain, which defined as $\eta = d_0 - d$, where $d_0 = 3.38$ Å is the optimized vertical distance. It can be seen from Fig. 1(c) that the binding energy increases rapidly with the increase of compressive strain, but very slowly with the increase of tensile strain. This is because the Coulomb repulsive force increases significantly with the decrease of interlayer spacing; on the contrary, the Coulomb attraction increases slowly with the increase of interlayer spacing.

Table 1

The calculated lattice constants a and b (Å), band gaps E_g (eV), and work function φ (eV).

Structure	$a = b$	E_g^{PBE}	E_g^{HSE06}	φ
Antimonene	4.04	1.42	1.91	4.82
C_3N	4.86	0.39	0.97	2.92
Antimonene/C_3N	8.38	0.15	0.59	3.40

The band structure of the heterojunction under different vertical strain is shown in Fig. 3(a). It can be seen that for the case of $\eta = -1.0$ Å, the band structure shows type-III arrangement with a band gap of zero. As the η increases, the band structure changes more significantly. In particular, when η increases to 0.8 Å, the charge exchange between bands is most obvious, and the sources of CBM and VBM are reversed. Specifically, the interlayer interaction between the C_3N and the antimonene is decreased with η decreasing from 0 to −1.0 Å, as a result, the charge transfer between C_3N and antimonene is significantly reduced, as demonstrated by the isosurface of the differential charge density in Fig. 3(b). It can be seen from Fig. 3(c) that the band gap shows a linear change with the vertical strain within a certain range, indicating that the band gap can be effectively controlled by strain engineering. Accordingly, the effect of η on potential drop ($\Delta\varphi$) is shown in Fig. 3(d).

For compressive strain, the increase of interfacial electron transfer enhances the built-in electric field E_{int} between C_3N and antimonene, resulting in the enhancement of interfacial electrostatic potential drop and corresponding increase of band gap. For tensile strain, the interfacial electron transfer is hindered, the built-in electric field decreases, the interfacial potential drop decreases, and the band gap decreases [26,27]. In addition, the electrostatic potential itself decreases with the decrease of layer spacing and increases with the increase of layer spacing, which is contrary to the change of electrostatic potential caused by strain. Therefore, it can be concluded that the reduction of electron transfer caused by tensile strain is the main reason for the decrease of electrostatic potential, compared with the change of electrostatic potential caused by the change of layer spacing. When the compression strain is less than 0.4 Å, the electron transfer caused by compression strain plays a dominant role in the competition. These results indicate that electrostatic potential difference is sensitive to the increase of layer spacing.

3.4. Adjustment of electronic structure by external electric field

In the application of nano-electronic devices, the gate voltage can effectively tune the electronic properties of materials [28,29]. To this end, the effect of E_{ext} on the electronic properties of the antimonene/C_3N heterostructure was explored. The positive direction of E_{ext} is from the C_3N to the antimonene, which is the same as the direction of E_{int}. We believe that the electronic properties of heterojunctions are jointly affected by E_{int} and E_{ext}. Evolution of the projected band structure of antimonene/C_3N bilayer with E_{ext} is shown in Fig. 4. The results show that under the influence of negative E_{ext}, the VBM of C_3N and the CBM of antimonene are closer to the Fermi level, while for positive E_{ext}, the situation is the opposite. As a result, the band gap of antimonene/C_3N bilayer decreases in the case of a negative E_{ext} and increases when subjected to a positive E_{ext}. Then, when the positive electric field increases to 0.25 $V \cdot Å^{-1}$, the antimonene/C_3N heterostructure changes from type-II to type-I. When the positive electric field is further increased to 0.35 $V \cdot Å^{-1}$, it can be found that a new band appeared in the conduction band, which was neither contributed by the C_3N layer, nor the antimonene layer. We believed that this phenomenon can be attributed to the formation of near free electrons (NFE) induced by a strong electric field [30]. With the existence of NFE, the band became the bottom of the conduction band and the heterojunction presents metallic properties.

Evolution of the band gap of antimonene/C_3N as a function of applied external E_{ext} is shown in Fig. 5(a). The results show that the band gap varies linearly with E_{ext}, which can be explained by the Giant Stark

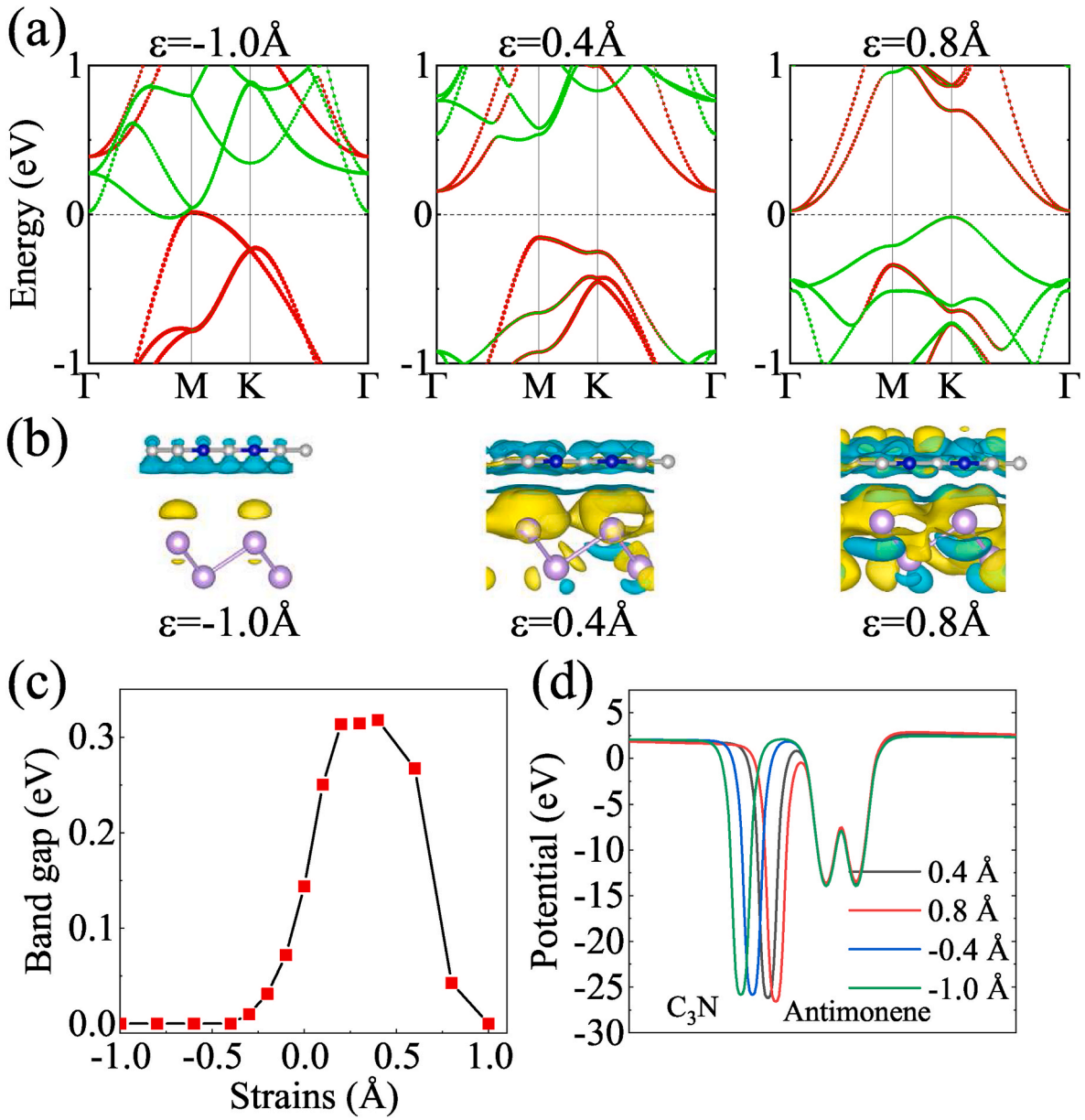

Fig. 3. (a) The band structure of the heterojunction under different vertical strain η based on PBE calculations. (b) The isosurface of the different charge density. The isovalue of the plot is 0.002e/Bohr^3. (c) The evolution of band gap as a function of η. (d) The electrostatic average potential for the antimonene/C_3N heterostructure under different η.

effect (GSE) [31]. Fig. 5(b) suggests that all the band edges also change linearly with the electric field. This phenomenon can be explained by the local electrostatic potential energy (LEPE) difference between layers, which is defined as $|e|(\vec{E}_{ext} + \vec{E}_{int})d_0$, in which the built-in electric field is very small and can be ignored compared with the external electric field [32]. Therefore, such interlayer LEPE can be regarded as determined by the applied electric field. When E_{ext} is positive, the LEPE of antimonene layer is higher than that of C_3N, so the CBM and VBM of antimonene layer move upward with the increase of electric field. When the electric field is negative, the situation is opposite, the LEPE of C_3N layer is higher, and the CBM and VBM in C_3N layer move upward with the increase of negative electric field. In order to further study how E_{ext} adjusts the electrical characteristics of the heterostructure, the integrated charge density is calculated by the following formula:

$$\Delta\rho_{E_{ext}}(z) = \int \rho_{E_{ext}}(x,y,z)dxdy - \int \rho_{E_0}(x,y,z)dxdy \quad (3)$$

where $\rho_{E_{ext}}(x,y,z)$ and $\rho_{E_0}(x,y,z)$ are the charge density at (x, y, z) point in the supercell of the antimonene/C_3N heterostructure with and without E_{ext}, respectively, are presented in Fig. 5(c). The integrated charge density can intuitively indicate that the stronger the negative electric field E_{ext}, the greater the amount of charge transfer. And it is worth emphasizing that the electrons always migrate from C_3N to antimonene. As the forward electric field increases, the number of electrons migrating from C_3N to antimonene decreases. The same evidence can be demonstrated by Fig. 5(d), when the heterojunction is under the positive E_{ext}, the balance of Fermi level is destroyed, and the Fermi level of C_3N moves down, while the Fermi level of antimonene moves up, resulting in the transfer of a certain number of electrons from antimonene to C_3N, the opposite is true when the heterojunction is subjected to a negative E_{ext}. Fig. 5(e) further shows the variation of the conduction band offset (CBO, defined by $\Delta E_C = E_{C(C_3N)} - E_{C(antimonene)}$) and valence band offset (VBO, defined by $\Delta E_V = E_{V(C_3N)} - E_{V(antimonene)}$) of the heterojunction with the applied E_{ext}. Both CBO and VBO decrease

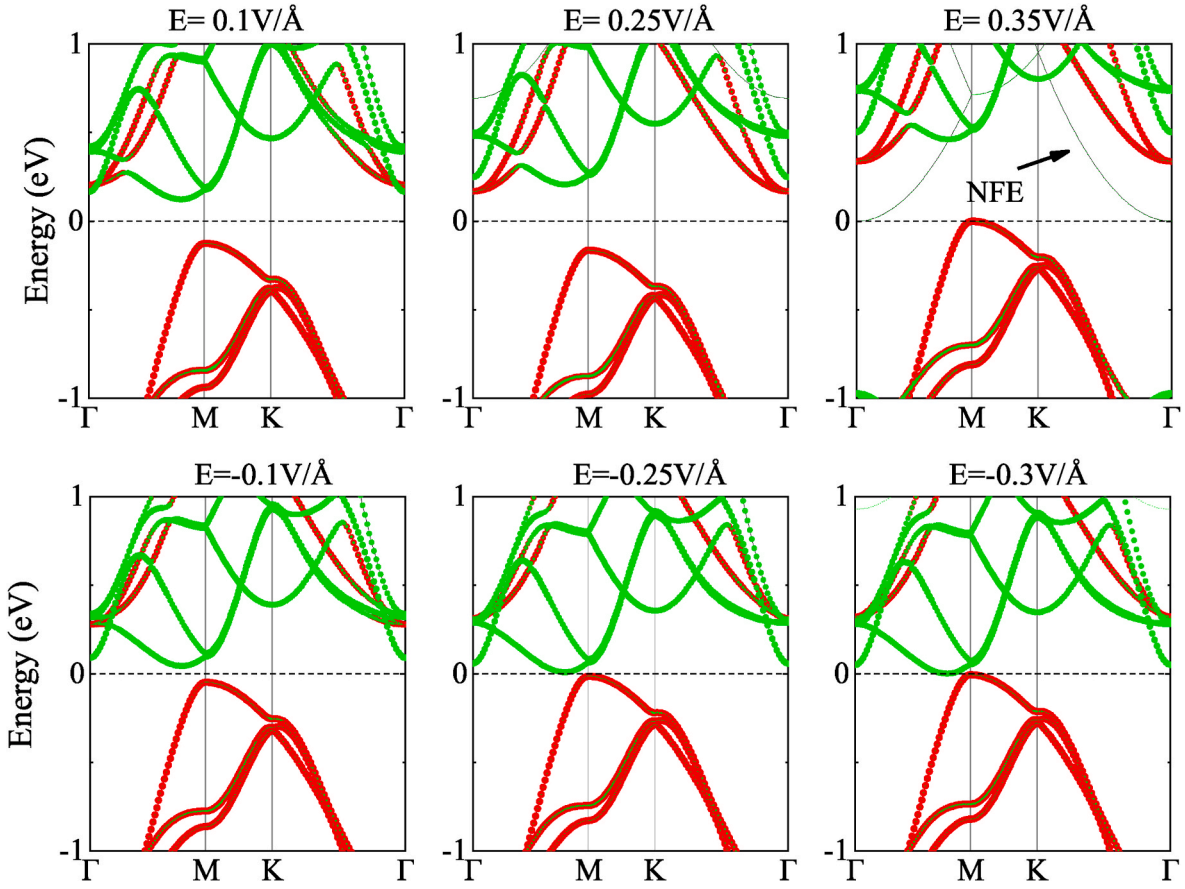

Fig. 4. The band structure of the antimonene/C_3N heterostructure under different E_{ext} based on PBE calculations.

with the increase of electric field, when $E_{ext} = -0.35$ V·A$^{\circ -1}$, $\Delta E_C = 0.33$ eV, $\Delta E_V = 1.41$ eV. Therefore, a larger negative electric field can provide a larger CBO and VBO and promote the separation of photogenerated electron hole pairs. And it can be seen that as the external electric field changes, the band gaps of C_3N ML and antimonene ML hardly change, but significant changes in charge transfer can be observed, as shown in Fig. 5(f). The increase of positive electric field hinders the charge transfer, while the negative electric field is beneficial to enhance the diffusion behavior of electrons and enhance the charge transfer. However, even at strong electric fields the amount of charge transfer is still very small due to weak van der Waals interactions between layers. The above results show that electrostatic gating can effectively act on the band gap adjustment of antimonene/C_3N heterostructure, which is beneficial for applications in high-performance electronic devices.

3.5. Optical properties

Due to the type-II energy band arrangement, photogenerated electrons and holes are effectively separated, which is essential for photocatalysis. Fig. 6(a) shows that the photogenerated holes in antimonene tend to flow to the valence band of C_3N, while the photogenerated electrons in C_3N tend to flow to the conduction band of antimonene. Therefore, the oxidation reaction occurs in the valence band of C_3N, and the reduction reaction occurs in the conduction band of antimonene. Fig. 6(b) shows that the C_3N/antimonene heterostructure can be designed as a photovoltaic cell. When sunlight is irradiated, light-excited electrons move to the positively charged N region (antimonene), and holes move to the negatively charged P region (C_3N). Through the charge separation of the interface layer, a measurable voltage will be generated between the P and N area.

Moreover, the optical properties of the antimonene/C_3N heterojunction have been explored. The calculated absorption coefficient and imaginary parts of the complex dielectric constant are shown in Fig. 7(a) and (b), respectively. The heterostructures exhibit a wide range of light absorption and maintain a high absorption coefficient even in the blue-light region, which is expected to be used in solar cells. The absorption coefficient in the blue range mainly comes from the contribution of antimonene, which is consistent with previous reports [11]. At the energy of 1.68 eV, 2.52 eV and 3.1 eV, three distinct absorption peaks can be observed, respectively. The vertical strain effects on the absorption coefficient has been calculated and shown in Fig. 7(c). When the applied vertical strain $\eta < 0$, the absorption spectrum red-shift occurs, while when the vertical strain $\eta > 0$, the absorption spectrum has a blue-shift. The effect of biaxial strain on the absorption curve is shown in Fig. 7(d). The biaxial strain can be expressed as $\eta' = (a\text{-}a_0)/a_0$, where a_0 and a are the lattice constant with and without stretching, respectively. Here, 1%–5% of the biaxial external tensile strain is applied. With the increase of the applied strain, the absorption spectrum has blue-shift and the intensity of absorption peak decrease.

4. Conclusion

In conclusion, we have systematically studied the electronic properties and optical performance of van der Waals antimonene/C_3N heterojunction by using DFT calculations. The antimonene/C_3N heterojunction forms a type-II heterojunction, which is conducive to the effective separation of photogenerated electron-hole pairs. In addition, the band structure can be effectively adjusted by electric field and vertical strain, both band gap and band edge change linearly with electric field. Then the heterojunction exhibits good optical performance in the visible light region, especially in the blue-light region, and the optical

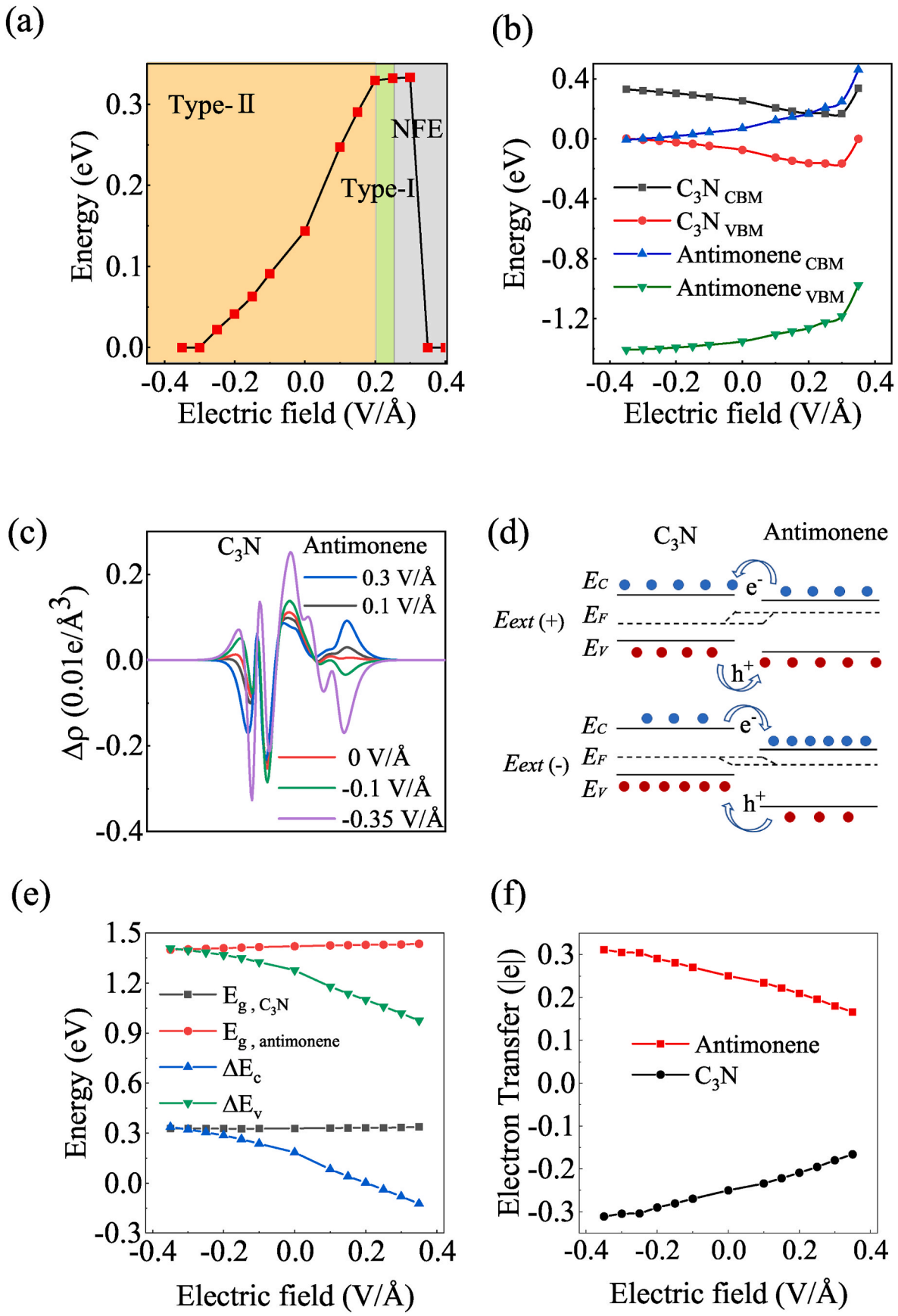

Fig. 5. The evolution of (a) the band gap and (b) the band edge as a function of E_{ext}. (c) The integrated charge density difference of the heterostructure under E_{ext}. (d) Band alignment of the antimonene/C_3N bilayer under positive and negative E_{ext}. (e) Band gaps for each layer, and band offset for heterostructure. (f) Electron transfer for each layer, the positive and negative values represent electron accumulation and depletion, respectively.

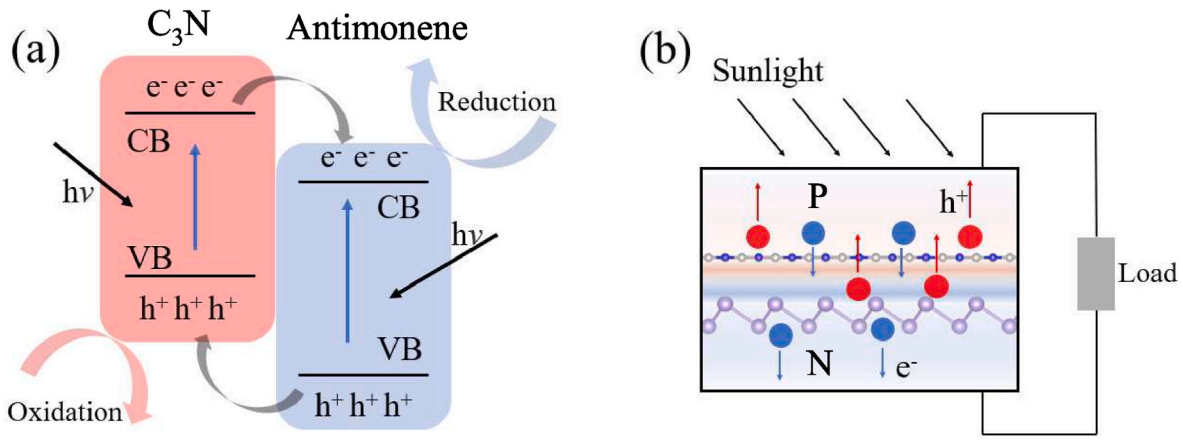

Fig. 6. (a) Band arrangement and electron migration mechanism of heterojunction. (b) Schematic diagram of C_3N/antimonene heterojunction photovoltaic device.

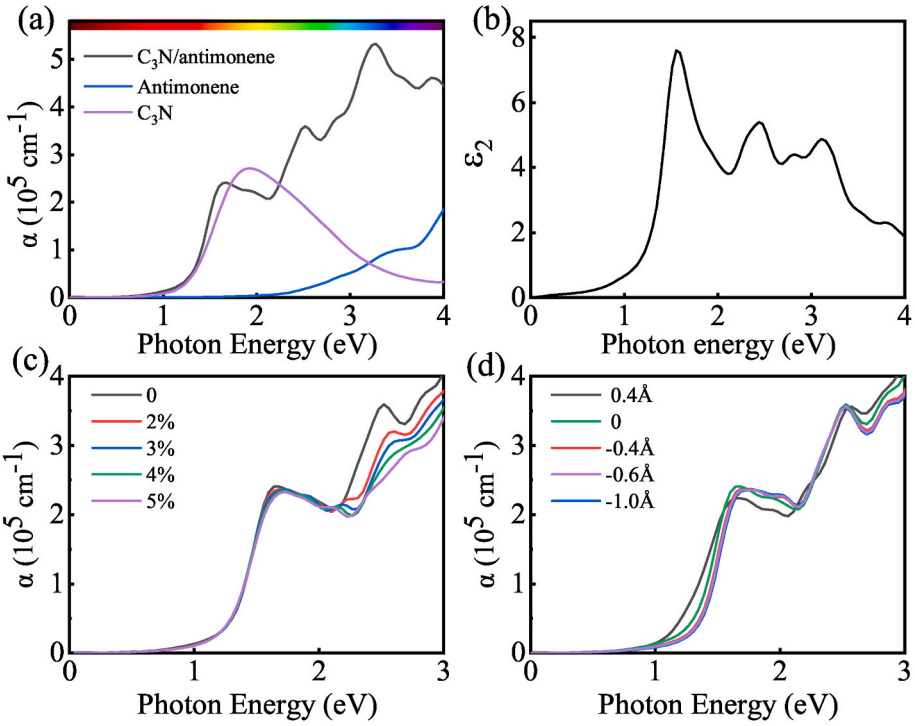

Fig. 7. (a) The absorption coefficient and (b) the imaginary part as a function of photon energy. The absorption coefficient as a function of (c) biaxial tensile strain η' and (d) vertical strain η.

properties can be adjusted by biaxial and vertical strain, which is expected to become a photovoltaic module for solar cells.

Author contribution statement

Lichen Gao: Conceptualization, Validation, Formal analysis, Writing – original draft preparation. **Bin Zhou:** Methodology, Formal analysis. **Jinzhong Zhang:** Methodology. **Kai Jiang:** Formal analysis. **Liyan Shang:** Methodology, Formal analysis. **Zhigao Hu:** Writing – review & editing, Supervision, Project administration, Funding acquisition. **Junhao Chu:** Funding acquisition.

Declaration of competing interest

The authors declare that they have no known competing financial interests or personal relationships that could have appeared to influence the work reported in this paper.

Acknowledgment

This work was financially supported by the National Natural Science Foundation of China (Grant Nos. 91833303, 61974043, 62074058, and 92090013), the National Key R&D Program of China (Grant No. 2019YFB2203403), the Projects of Science and Technology Commission of Shanghai Municipality (Grant Nos. 18JC1412400, 18YF1407200, 18YF1407000 and 19511120100), the Program for Professor of Special Appointment (Eastern Scholar) at Shanghai Institutions of Higher Learning and Shanghai Pujiang Program (20PJ1403600).

References

[1] K.S. Novoselov, A.K. Geim, S.V. Morozov, D. Jiang, Y. Zhang, S.V. Dubonos, I. V. Grigorieva, A.A. Firsov, Electric field effect in atomically thin carbon films, Science 306 (2004) 666–669, https://doi.org/10.1126/science.1102896.
[2] K. Alhassoon, M. Han, Y. Malallah, V. Ananthakrishnan, R. Rakhmanov, W. Reil, Y. Gogotsi, A. Daryoush, Conductivity extraction of thin $Ti_3C_2T_x$ MXene films over

1-10 GHz using capacitively coupled test-fixture, Appl. Phys. Lett. 116 (2020) 184101, https://doi.org/10.1063/5.0002514.
[3] H. Yao, E. Wu, J. Liu, Frequency doubler based on a single $MoTe_2/MoS_2$ anti-ambipolar heterostructure, Appl. Phys. Lett. 117 (2020) 123103, https://doi.org/10.1063/5.0018882.
[4] Y.D. Ma, D. Ying, C.W. Niu, B.B. Huang, Halogenated two-dimensional germanium: candidate materials for being of Quantum Spin Hall state, J. Mater. Chem. 22 (2012) 12587–12591, https://doi.org/10.1039/C2JM30960B.
[5] L.K. Li, Y.J. Yu, G.J. Ye, Q.Q. Ge, X.D. Ou, H. Wu, Black phosphorus field-effect transistors, Nat. Nanotechnol. 9 (2014) 372–377, https://doi.org/10.1038/nnano.2014.35.
[6] S. Sucharitakul, N. Goble, U. Kumar, R. Sankar, Z. Bogorad, F.C. Chou, Y.T. Chen, X. Gao, Intrinsic electron mobility exceeding 10^3 $cm^2/(V\,s)$ in multilayer InSe FETs, Nano Lett. 15 (2015) 3815–3819, https://doi.org/10.1021/acs.nanolett.5b00493.
[7] S.W. Yang, W. Li, C.C. Ye, G. Wang, H. Tian, C. Zhu, P. He, G.Q. Ding, X.M. Xie, Y. Liu, Y. Lifshitz, S.T. Lee, Z.H. Kang, M.H. Jiang, C_3N-a 2D crystalline, hole-free, tunable-narrow-bandgap semiconductor with ferromagnetic properties, Adv. Mater. 29 (2017) 1605625, https://doi.org/10.1002/adma.201605625.
[8] Y. Qie, J.Y. Liu, S. Wang, S. Gong, Q. Sun, C_3B monolayer as an anchoring material for lithium-sulfur batteries, Carbon 129 (2018) 38–44, https://doi.org/10.1016/j.carbon.2017.11.068.
[9] J.T. Xu, J. Mahmood, Y.H. Dou, S.X. Dou, F. Li, L.M. Dai, J.B. Baek, 2D frameworks of C_2N and C_3N as new anode materials for Lithium-ion batteries, Adv. Mater. 29 (2017) 1702007, https://doi.org/10.1002/adma.201702007.
[10] X. Wu, Y. Shao, H. Liu, Z.L. Feng, Y.L. Wang, Epitaxial growth and air-stability of monolayer antimonene on $PdTe_2$, Adv. Mater. 29 (2017) 1605407, https://doi.org/10.1002/adma.201605407.
[11] J.P. Ji, X.F. Song, J.Z. Liu, Z. Yan, C.X. Huo, S.L. Zhang, M. Su, L. Liao, W.H. Wang, Z.H. Ni, H.B. Zeng, Two-dimensional antimonene single crystals grown by van der Waals epitaxy, Nat. Commun. 6 (2016) 13352, https://doi.org/10.1038/ncomms13352.
[12] L. Lu, X. Tang, R. Cao, L.M. Wu, Z.J. Li, G.H. Jing, B.Q. Dong, S.B. Lu, Y. Li, Y. J. Xiang, J.Q. Li, D.Y. Fan, H. Zhang, Broadband nonlinear optical response in few-layer antimonene and antimonene quantum dots: a promising optical kerr media with enhanced stability, Adv. Opt. Mater. 5 (2017) 1700301, https://doi.org/10.1002/adom.201700301.
[13] G.G. Kresse, J. Hafne, Ab initio molecular dynamics for liquid metals, Phys. Rev. B 47 (1993) 558, https://doi.org/10.1103/PhysRevB.47.558.
[14] G.G. Kresse, J.J. Furthmuöller, Efficient iterative schemes for ab initio total-energy calculations using a plane-wave basis set, Phys. Rev. B 54 (1996) 11169, https://doi.org/10.1016/0927-0256(96)00008-0.
[15] J. Perdew, K. Burke, M. Ernzerhof, Generalized gradient approximation made simple [Phys. Rev. Lett. 77, 3865 (1996)], Phys. Rev. Lett. 78 (1997) 1396, https://doi.org/10.1103/PhysRevLett.78.1396.
[16] J. Klimes, D.R. Bowler, A. Michaelides, Van der Waals density functionals applied to solids, Phys. Rev. B 83 (2011) 195131, https://doi.org/10.1103/physrevb.83.195131.
[17] H.J. Monkhorst, J.D. Pack, Special points for Brillouin-zone integrations, Phys. Rev. B 13 (1976) 5188, https://doi.org/10.1103/PhysRevB.13.5188.
[18] M. Gajdos, K. Hummer, G. Kresse, J. Furthmüller, F. Bechstedt, Linear optical properties in the projector-augmented wave methodology, Phys. Rev. B 73 (2006), 045112, https://doi.org/10.1103/PhysRevB.73.045112.
[19] L. Tan, C.Y. Nie, Z.M. Ao, H.Q. Sun, T.C. An, S.B. Wang, Novel two-dimensional crystalline carbon nitrides beyond g-C_3N_4: structure and applications, J. Mater. Chem. A. 9 (2021) 17–33, https://doi.org/10.1039/D0TA07437C.
[20] T.F. Cheng, L. Li, L.Y. Li, Y.N. Zhang, Y.H. Gao, Linear regulation of electrical characteristics of InSe/antimonene heterojunction via external electric field and strain, Surf. Interfaces. 23 (2021) 101014, https://doi.org/10.1016/j.surfin.2021.101014.
[21] H. Zeng, J. Zhao, A.Q. Cheng, L. Zhang, Z. He, R.S. Chen, Tuning electronic and optical properties of arsenene/C_3N van der Waals heterostructure by vertical strain and external electric field, Nanotech 29 (2018), 075201, https://doi.org/10.1088/1361-6528/aaa2e8.
[22] Y. Cai, G. Zhang, Y.W. Zhang, Layer-dependent band alignment and work function of few-layer phosphorene, Sci. Rep. 4 (2014) 6677, https://doi.org/10.1038/srep06677.
[23] C. Kaewmeechai, Y. Laosiritaworn, A. Jaroenjittichai, DFT band alignment of polar and nonpolar GaN/$MgGeN_2$, ZnO/$MgGeN_2$ and GaN/ZnO heterostructures for optoelectronic device design, Appl. Surf. Sci. 533 (2020) 147503, https://doi.org/10.1016/j.apsusc.2020.147503.
[24] B. Zhou, K. Jiang, L.Y. Shang, J.J. Zhang, Y.W. Li, L.Q. Zhu, S.J. Gong, Z.G. Hu, J. H. Chu, Enhanced carrier separation in ferroelectric In_2Se_3/MoS_2 van der Waals heterostructure, J. Mater. Chem. C. 8 (2020) 11160, https://doi.org/10.1039/D0TC02366C.
[25] P. Wang, Y.X. Zong, L. Hao, H.Y. Wen, Y.Y. Liu, H.B. Wu, J.B. Xia, Vertical strain and electric field tunable band alignment in type-II ZnO/MoSSe van der Waals heterostructures, Nanotech 23 (2021) 1510–1519, https://doi.org/10.1039/D0CP05354F.
[26] P.F. Yuan, J.N. Han, Z.Q. Fan, Z.H. Zhang, C.Z. Wang, Stable C_2N/h-BN van der Waals heterostructure: flexibly tunable electronic and optic properties, J. Phys.: Condens. Mater. 32 (2020) 475001, https://doi.org/10.1088/1361-648X/abaf12.
[27] J.K. Hu, J.X. Tan, D. Wu, Z.H. Zhang, Z.Q. Fan, Exploring magnetic stability and valley splitting on CrI_3/SiC van der Waals heterostructure, Appl. Surf. Sci. 560 (2021) 149858, https://doi.org/10.1016/j.apsusc.2021.149858.
[28] C. Yu, Z. Wang, Strain engineering and electric field tunable electronic properties of Janus MoSSe/WX_2 (X=S, Se) van der Waals heterostructures, Phys. Status Solidi B 256 (2019) 1900261, https://doi.org/10.1002/pssb.201900261.
[29] L. Huang, N.J. Huo, Y. Li, H. Chen, J.H. Yang, Z.M. Wei, J.B. Li, S.S. Li, Electric-field tunable band offsets in black phosphorus and MoS_2 van der Waals p-n heterostructure, J. Phys. Chem. Lett. 6 (2015) 2483–2488, https://doi.org/10.1021/acs.jpclett.5b00976.
[30] B. Zhou, K. Jiang, L.Y. Shang, J.J. Zhang, L.P. Xu, S.J. Gong, Z.G. Hu, J.H. Chu, A type-II GaSe/GeS heterobilayer with strain enhanced photovoltaic properties and external electric field effects, J. Mater. Chem. C. 8 (2020) 89–97, https://doi.org/10.1039/C9TC05840K.
[31] L. Huang, M.Z. Zhong, H.X. Deng, B. Li, Z.M. Wei, J.B. Li, S.H. Wei, The coulomb interaction in van der Waals heterostructures, Sci. China. Phys. Mech. 62 (2019) 37311, https://doi.org/10.1007/s11433-018-9294-4.
[32] Y.H. Xu, Z.Q. Fan, Z.H. Zhang, T. Zhao, Electronic and transport properties of GaAs/InSe van der Waals heterostructure, Appl. Surf. Sci. 547 (2021) 149174, https://doi.org/10.1016/j.apsusc.2021.149174.